

Article

High-Temperature Elastic Properties of Yttrium-Doped Barium Zirconate

Fumitada Iguchi ^{1,2,*}  and Keisuke Hinata ²

¹ College of Engineering, Nihon University, 1, Nakagawara, Tokusada, Tamura, Koriyama, Fukushima 963-8642, Japan

² Graduate School of Engineering, Tohoku University, 6-6-01, Aoba, Aramaki, Aoba-ku, Sendai, Miyagi 980-8579, Japan; keisuke.hinata.s4@dc.tohoku.ac.jp

* Correspondence: Iguchi.fumitada@nihon-u.ac.jp; Tel.: +81-24-956-8784

Abstract: The elastic properties of 0, 10, 15, and 20 mol% yttrium-doped barium zirconate (BZY0, BZY10, BZY15, and BZY20) at the operating temperatures of protonic ceramic fuel cells were evaluated. The proposed measurement method for low sinterability materials could accurately determine the sonic velocities of small-pellet-type samples, and the elastic properties were determined based on these velocities. The Young's modulus of BZY10, BZY15, and BZY20 was 224, 218, and 209 GPa at 20 °C, respectively, and the values decreased as the yttrium concentration increased. At high temperatures (>20 °C), as the temperature increased, the Young's and shear moduli decreased, whereas the bulk modulus and Poisson's ratio increased. The Young's and shear moduli varied nonlinearly with the temperature: The values decreased rapidly from 100 to 300 °C and gradually at temperatures beyond 400 °C. The Young's modulus of BZY10, BZY15, and BZY20 was 137, 159, and 122 GPa at 500 °C, respectively, 30–40% smaller than the values at 20 °C. The influence of the temperature was larger than that of the change in the yttrium concentration.



Citation: Iguchi, F.; Hinata, K.

High-Temperature Elastic Properties of Yttrium-Doped Barium Zirconate.

Metals **2021**, *11*, 968. <https://doi.org/10.3390/met11060968>

Academic Editor: Huaiyu Shao

Received: 24 May 2021

Accepted: 11 June 2021

Published: 16 June 2021

Publisher's Note: MDPI stays neutral with regard to jurisdictional claims in published maps and institutional affiliations.



Copyright: © 2021 by the authors. Licensee MDPI, Basel, Switzerland. This article is an open access article distributed under the terms and conditions of the Creative Commons Attribution (CC BY) license (<https://creativecommons.org/licenses/by/4.0/>).

Keywords: solid oxide fuel cell (SOFC); solid oxide electrolyzer cell (SOEC); proton conductor; perovskite; defect structure; hydration; oxygen vacancy; Young's modulus; Poisson's ratio

1. Introduction

To address the critical issues pertaining to global climate change, the realization of efficient and environmentally friendly energy utilization and conversion has attracted increasing research attention. Several devices are being developed to encourage the utilization of renewable energy sources and reduce the consumption of fossil fuels and emission of CO₂. In this regard, solid oxide fuel cells (SOFCs) are key representative devices owing to the associated high efficiency of electrochemical energy conversion (from chemical to electrical energy) and high fuel flexibility resulting from their operating temperature being more than 700 °C. Moreover, SOFCs can operate as solid oxide electrolyzer cells that convert electrical energy into chemical energy; in other words, SOFCs realize reversible electrochemical energy conversion. However, owing to the high operating temperature, SOFCs encounter issues pertaining to long-term mechanical and chemical stability. Protonic ceramic fuel cells (PCFCs) are promising devices that operate at a lower temperature (400–600 °C) than that of commercially developed SOFCs and thus exhibit a high flexibility in component materials along with a longer operational lifetime [1,2]. The low operating temperature of PCFCs is a result of the high protonic conductivity of protonic ceramics, which is a result of the smaller activation energy required for proton transport [3–5]. Numerous researchers have focused on PCFCs and their applications as highly efficient energy conversion devices and attempted to develop the associated component materials [6–17].

During the operation of conventional SOFCs, a high mechanical stability must be ensured. Consequently, the stress conditions and mechanical stability of SOFCs and constituent materials have been widely examined [18–29]. Although PCFCs operate at

a lower temperature than that of SOFCs, large thermal stresses are introduced owing to the several thermal cycles during operations. Moreover, the residual stresses induced in the fabrication process typically remain in the PCFCs. In addition, proton-conducting electrolytes, such as yttrium-doped BaZrO₃ and BaCeO₃, have a lower thermal expansion coefficient (TEC) than that of oxygen-ion-conducting electrolytes, such as yttria-stabilized zirconia (YSZ) [30–32]. Furthermore, the lattice volume of protonic ceramics expands during hydration, which is a type of chemical expansion caused by the changes in the defect structure [32,33]. Consequently, the thermal stresses in PCFCs are likely considerably larger than those in SOFCs owing to the more notable TEC mismatch between the proton-conducting electrolyte and other components, such as the electrodes. This aspect, in addition to the large chemical stress induced during hydration, leads to differential stress and deformation in a cell during operation. Moreover, the current PCFC architecture involves primarily anode-supported or metal-supported cell structures; specifically, porous metal substrates are introduced in metal-supported cells, whereas anode-supported cells include thicker anodes in the structure [7,34–37]. As the elastic performance of ductile metals is different than that of brittle ceramics, the mechanical properties and stress conditions in these two architectures differs considerably. Therefore, to realize mechanically and chemically stable cells, it is necessary to evaluate the in situ mechanical stability, stress conditions, and amount of deformation in PCFCs.

To analyze the stress conditions and deformation in cells, the elastic properties of each constituent material under various temperatures and environments must be determined as fundamental mechanical properties to clarify the deformation response to applied forces. Several PCFC constituent materials have been developed, especially for the proton-conducting ceramic electrolytes; however, the elastic properties of the proton-conducting ceramics remain unclear, although certain researchers have attempted to experimentally clarify these elastic properties [38,39]. In particular, yttrium-doped barium zirconate (BZY) is a representative perovskite-type proton-conducting electrolyte with a high chemical stability and reasonable proton conductivity in the temperature range of 400–600 °C [40,41]. Although the electrochemical performance and thermochemical properties of BZY, such as the TEC, have been reported [32,33], its elastic properties at the operating temperature remain unclear.

A key challenge in the experimental investigation of BaZrO₃-based ceramics is the preparation of stable samples, as the materials exhibit a low sinterability [42,43]. The fabrication of dense BZY samples by using the solid-state reaction method requires a sintering temperature that is considerably higher than 1600 °C in the absence of sintering aids, which makes it difficult to prepare a large sample or a sample with precise dimensions. In this regard, small samples such as pellets, which are commonly used in electrochemical investigations, can be used to examine the elastic properties. Conventional methods for elastic properties investigation are classified to static and dynamic tests, respectively. Static tests, such as tensile, compression, and bending tests, are usually performed using mechanical testing machines and thus relatively large samples [28,44]. In contrast, in dynamic tests, such as ultrasonic and resonance tests, small samples can be used to investigate the elastic properties. The resonance method involves limitations in terms of the sample shape and the requirement of samples with precise dimensions. The ultrasonic method, however, can be applied using samples of any size, with none of the sample-related limitations involved in the resonance method.

In the ultrasonic method, longitudinal and transverse ultrasonic sounds are used. Four elastic constants—the Young's, shear, and bulk moduli and the Poisson's ratio—can be obtained by measuring the sound velocities of the longitudinal and transverse waves. The velocity of sound in the sample is obtained by dividing the propagated length of the ultrasonic waves by the propagated time, which is often termed as the time-of-flight (TOF) and can be measured using the two-probe transmission or one-probe echo method. In the former method, the TOF is determined by considering the difference in the transmission and receiving time of two probes that sandwich the samples. In the latter method, the TOF

is determined by the gap of reflections transmitted by one probe attached to one side of the samples. Although the same result is obtained using both the approaches, the accuracy of the measurement using one probe tends to be higher than that of two probes because multiple reflections can be used for the calculation if the attenuation rate in the samples is extremely low. This aspect is particularly important/relevant as the attenuation in protonic ceramics is considerably higher than that in fused silica or stainless steel, which makes the use of the two-probe approach more suitable than that of the one-probe approach under high temperature measurement settings.

Furthermore, in the context of high-temperature measurements, the probes must be protected from the high-temperature samples. In general, approaches for high-temperature measurements involve rods named buffer rods or waveguides, which are made of heat resistant materials with a low attenuation rate. These rods connect the probe and the sample and transmit ultrasonic waves between them [45]. In the one-probe method, the TOF is measured by considering the reflection return times from both ends of the samples. However, a preliminary study indicated that the wave intensity of the reflection from the opposite side of the sample was significantly attenuated owing to the high attenuation rate in the BZY, whose thickness was limited owing to its low sinterability [42,46], and the attenuation in the solid–solid interface between the sample and a buffer rod made of a stainless steel bolt. Specifically, the first reflection waves interfered with the reflection waves from the probe side surface, and the second reflection waves were hidden by the noise from the side wall of the buffer rod. Furthermore, samples with a sufficiently large thickness (more than tens of millimeters) cannot be prepared, and thus, the interference between the reflection waves from both ends cannot be prevented when using the existing equipment.

In this study, considering this background, the elastic properties of BZYs with different doping amounts were examined as a function of temperature up to 600 °C. To overcome the limitations of the existing measurement approach, a novel approach based on the buffer rod technique to measure high-temperature ultrasonic sound velocities by using a small pellet and two buffer rods, according to the two-probe method, was developed. We briefly reported the results of high temperature measurements for doped barium zirconate [47]. After that, we conducted an additional experiment and obtained interesting observations about the temperature dependence of elastic properties. Therefore, in this paper, we report the systematic experimental results thus far. To the best of the authors' knowledge, our study is the first to report on the high-temperature elastic properties of BZY.

2. Materials and Methods

To evaluate the elastic properties of BZY, BZY pellets with various concentrations of yttrium were prepared using the solid-state reaction method: BaZrO_3 (BZY0), $\text{BaZr}_{0.90}\text{Y}_{0.10}\text{O}_{3-\delta}$ (BZY10), $\text{BaZr}_{0.85}\text{Y}_{0.15}\text{O}_{3-\delta}$ (BZY15), and $\text{BaZr}_{0.80}\text{Y}_{0.20}\text{O}_{3-\delta}$ (BZY20). In particular, BaCO_3 (> 99.99%, Rare Metallic Co., Ltd., Tokyo, Japan), ZrO_2 (Tosoh Co., TZ-0), and Y_2O_3 (99.999%, Nippon Yttrium Co., Ltd., Fukuoka, Japan) powders were mixed in the prescribed mole ratio and milled using a planetary ball mill (Fritsch Co., Idar-Oberstein, Germany, Pulverisette 6) for 24 h with a mixture of ethanol and isopropanol (Japan Alcohol Trading Co., Ltd., Tokyo, Japan, AP-7). Subsequently, the dried powders were calcined at 1380 °C for three hours and ball-milled again for 24 h. The BZY powders were consolidated using a 25 MPa uniaxial press and 220 MPa isostatic press to generate a thin cylinder. The formed pellets of BZY10, 15, and 20 were sintered in a zirconia high-temperature furnace (Shinagawa Refractories Co., Ltd., Tokyo, Japan, ZRF-25) at 1800 °C for 20 h in air, and BZY0 was sintered at 1600 °C for 10 h in air using a conventional electric furnace. The sintered BZY pellets were polished using diamond pads to remove the outer Ba-evaporated layer (ca. 500 μm), and this aspect was verified via X-ray diffraction (XRD) performed using an X-ray diffractometer (PANalytical, Malvern, UK, X'Pert Pro). Finally, pellet type samples with a thickness of approximately 5 mm were obtained. The crystal structure and lattice parameters were determined by XRD measurement after the completion of the polishing. The metric densities of the samples were determined by measuring the dimensions and

mass of the sample, and the values were crosschecked using the Archimedes method. The details of preparation and characterization was reported elsewhere [4,40,48].

The temperature dependence of the elastic moduli was examined by means of the ultrasonic method implemented using the apparatus shown in Figure 1. The sample was fixed between two buffer rods, and the interfaces between the sample and the buffer rod were connected by applying Ag paste (Aremco Products Inc., New York, USA, Aremco-Bond 525). A stainless steel bolt ($\phi 15$ mm, length 150 mm) was used as the buffer rod, as a threaded plane can suppress the undesirably strong reflection from the side wall of the buffer rod [49]. Ultrasonic waves were transmitted and received by two types of ultrasonic probes for longitudinal waves (Japan Probe Co., Ltd., Yokohama, Japan, 2C15N) and transverse waves (Japan Probe Co., Ltd., Yokohama, Japan, 2Z 10 \times 10 SN), controlled by the ultrasonic pulser-receiver (Japan Probe Co., Ltd., Yokohama, Japan, JPR-10CN). The frequency of the ultrasonic waves was 2.0 MHz. Ultrasonic probes were placed in secure contact with the upper and lower buffer rods using a couplant for longitudinal waves (Olympus Co. Couplant B2) and transverse waves (Taiyo Nippon Sanso Co., Ltd., Tokyo, Japan, Soni-coat SHN-B25), respectively. The sample was heated using an electric heater, and the outer ends of the buffer rods were maintained at a temperature less than 40 °C, which is the upper temperature limit of the ultrasonic couplant, through cooling from water-cooling jackets during the high-temperature measurement.

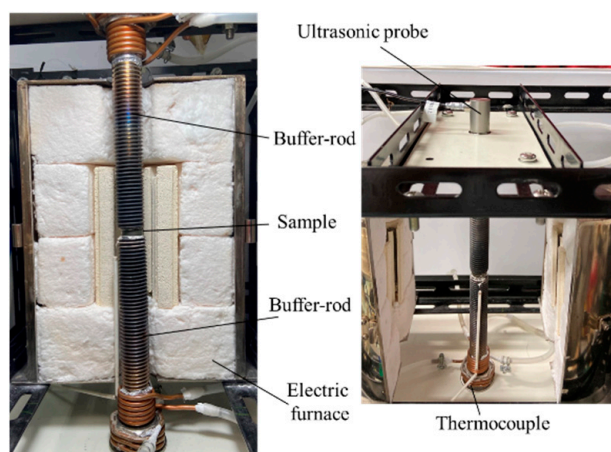


Figure 1. Photograph of experimental apparatus. The sample was set between two buffer rods in the electric furnace to measure the ultrasonic time-of-flight in the sample at high temperature.

The schematic of the measurement approach is shown in Figure 2. The sound velocities were obtained by considering the sample thickness and TOF in the sample (T_S). To obtain T_S , the compensation of the TOF in the two buffer rods from the total TOF was required. The ratio of the passing length of the two buffer rods to the thickness of the sample was approximately 60. Therefore, highly accurate compensation was required to ensure the accuracy of T_S . At room temperature (20 °C), a simple compensation using the length of the two buffer rods and the velocity of sound in stainless steel could help realize the highly accurate measurement of the sound velocity, with the error of the velocities lying within $\pm 2\%$. However, a preliminary study indicated that the large temperature gradient from the sample to the probe generated a sound velocity gradient in the buffer rods, because the sound velocities changed according to the temperature [45]. Furthermore, the reflectance and transmittance of the interfaces between the buffer rod and the sample connected by the Ag-bonded layer likely changed at a high temperature owing to the change in the mechanical properties of Ag. The aforementioned simple method could not compensate for these changes and was expected to yield a large measurement error.

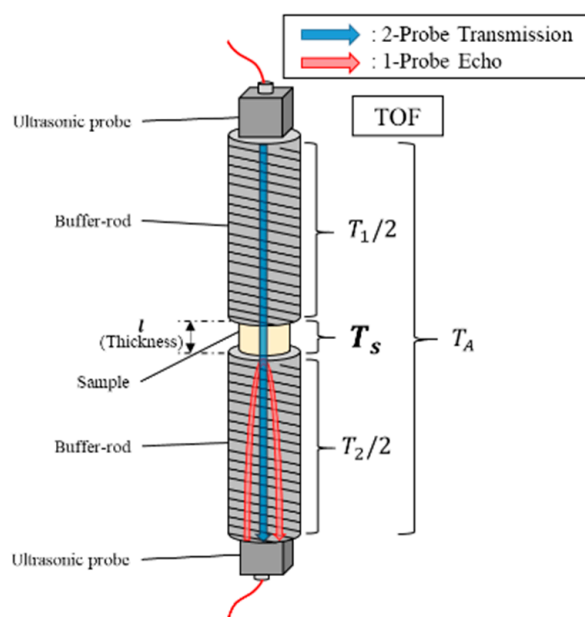


Figure 2. Concept of proposed measurement method for small pellet samples. The method is a combination of the 2-probe transmission method and 1-probe echo method. The transmitted ultrasonic waves (blue arrow) propagate between two probes, and the ultrasonic echoes (red arrow) are transmitted and detected by a probe.

Therefore, an alternative compensation process was applied. First, the TOF of ultrasonic sound propagating through the two buffer rods and the sample (T_A) was measured using the 2-probe method. Subsequently, the round trip TOFs of the ultrasonic sound propagating in the upper and lower buffer rods (T_1 and T_2 , respectively) were measured using the 1-probe method. Assuming T_A , T_1 , and T_2 could be measured in a reasonably brief period involving a negligible temperature change, T_1 and T_2 could be considered to include the influence of the sound velocity gradient caused by the temperature gradient, and highly accurate T_S could be obtained using Equation (1). The sound velocities V were calculated as shown in Equation (2), using the measured T_S and sample thickness L :

$$T_S = T_A - \frac{T_1 + T_2}{2} \quad (1)$$

$$V = \frac{L}{T_S} \quad (2)$$

Using this method, the sound velocities of fused silica [50] were measured, and it was confirmed that the error of the sound velocities was within $\pm 5\%$.

In addition to the effect of the temperature, it was necessary to consider the effect of the porosity, as BZY is not completely dense as compared with fused silica. In the applied preparation method, the sample porosity was expected to range from 1 to 5% and to decrease the sound velocity by a maximum of 5%. Thus, it was necessary to take into account the influence of porosity to suitably characterize the elastic properties of the sample. To this end, empirical equations were used to clarify the dependence of the sound velocities on the porosity P in 8 mol% YSZ (8YSZ) with porosities varying up to 20%, as shown in Figure S1. Using these values, the longitudinal and transverse sound velocities V_L and V_T could be determined using Equations (3) and (4), respectively:

$$V_L = V / (1 - 0.01034P) \quad (3)$$

$$V_T = V / (1 - 0.00839P) \quad (4)$$

Subsequently, V_L and V_T in BZY0, BZY10, BZY15, and BZY20 were measured using the experimental apparatus shown in Figure 1, according to the aforementioned modified method. The samples were heated in a furnace from 20 °C to 700 °C in increments of 50 °C. The actual sample temperature was measured using a K-type thermocouple located near the samples. As shown in Figure 1, the furnace and sample were exposed to the air-conditioned laboratory air (20 °C). Therefore, the measurement environment was considered to be that of noncontrolled low humidified air.

Based on the two velocities, the Young's modulus E , shear modulus G , Poisson's ratio ν , and bulk modulus K were calculated using Equations (5)–(8), respectively, where ρ was the theoretical density of the prepared samples, calculated from the lattice parameters determined using the XRD technique:

$$E = \frac{\rho V_T^2 (3V_L^2 - 4V_T^2)}{V_L^2 - V_T^2} \quad (5)$$

$$G = \rho V_T^2 \quad (6)$$

$$\nu = \frac{V_L^2 - 2V_T^2}{2(V_L^2 - V_T^2)} \quad (7)$$

$$K = \frac{E}{3(1 - 2\nu)} \quad (8)$$

3. Results and Discussion

The obtained BZY0, BZY10, BZY15, and BZY20 samples for the ultrasonic measurements were sufficiently dense and thick, and they remained stable through the high-temperature measurements. All the peaks in the XRD patterns of all the samples corresponded to a cubic perovskite-type structure (Fm-3m), as shown in Figure 3a. The calculated lattice parameters are listed in Table 1. These lattice parameters were in agreement with the values reported in previous literature [33,48]. Although the employed sintering temperature (1800 °C) was not the same as that generally employed for BZY (less than 1600 °C), they can be considered equivalent from the viewpoint of crystal structures. According to the designed chemical compositions and lattice parameters, the theoretical density was calculated, and the porosity was obtained by comparing the metric densities of the prepared samples. The typical microstructure of the prepared samples is shown in Figure 3b. The surface image taken by a scanning electron microscope (SEM: Hitachi High-Tech Corp., Tokyo, Japan, SU-70)) of BZY20, chemically etched using a colloidal silica followed by mechanical polishing, revealed that this sample was dense, and grain was well connected without the indication of any precipitations at grain boundaries. All samples showed similar microstructures except for grain size. The grain size of the prepared samples measured by the line-intercept method was 1.9, 1.7, 2.8, and 6.8 μm for BZY0, 10, 15, and 20, respectively.

Table 1. Thickness, lattice parameters, theoretical density, porosity, and average grain size of the samples.

Abbreviation	Thickness (mm)	Lattice Parameter (Å)	Theoretical Density (gcm^{-3})	Porosity (%)	Ave. Grain Size (μm)
BZY0	4.98	4.194	6.23	5.4	1.9
BZY10	5.87	4.207	6.15	6.2	1.7
BZY15	6.44	4.214	6.11	6.1	2.8
BZY20	4.30	4.223	6.05	6.1	6.8

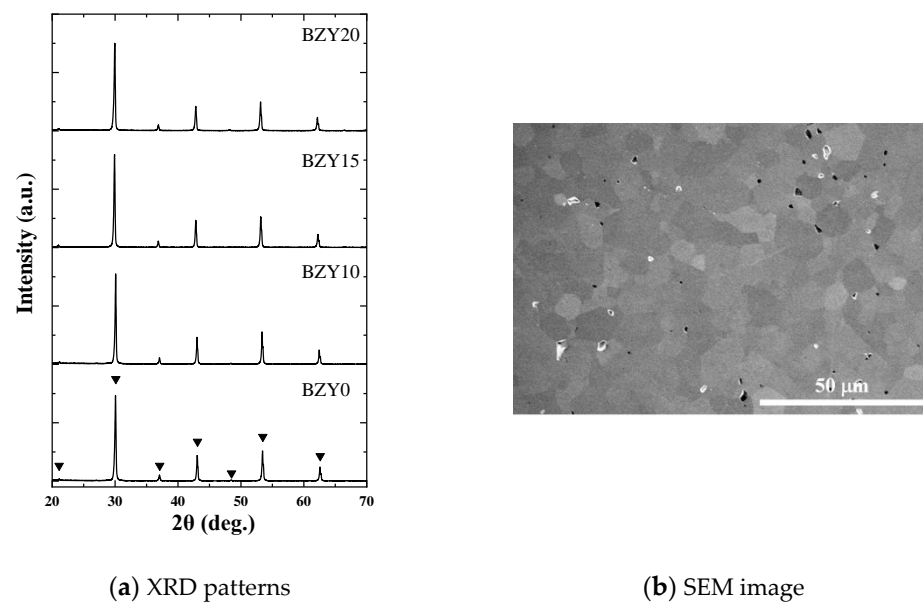
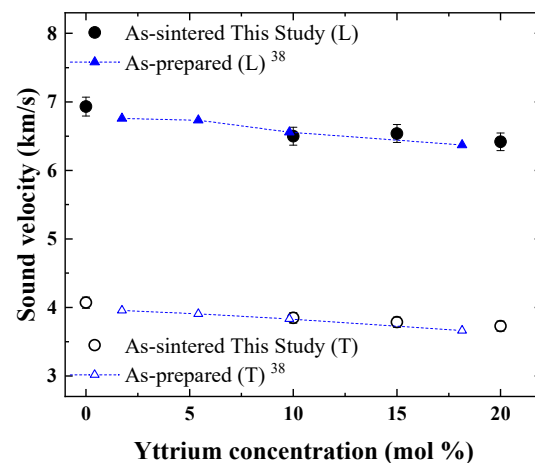
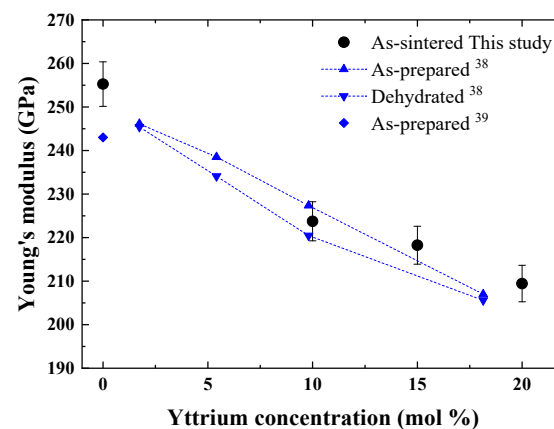


Figure 3. (a) XRD patterns of sintered BZY0, BZY10, BZY15, and BZY20 samples. Triangles indicate the 2θ of XRD peaks of BaZrO_3 according to JCPDS 00-006-0399. (b) SEM image of BZY20 surface chemically etched using colloidal silica followed by mechanical polishing. The microstructures in BZY0, BZY10, BZY15 are similar to those in BZY20 except for grain size.

The sound velocities of the prepared samples were measured at room temperature ($20\text{ }^\circ\text{C}$) by using the two-probe method without the buffer rods to enable a comparison with the reported values. Figure 4a shows the longitudinal and transverse sound velocities of the prepared samples as a function of the yttrium concentration with the velocities of BZY with a yttrium concentration of 1.5, 5.5, 10, and 17.5 mol% reported by Hoedl et al. [38], who correlated the influence of porosity using a dynamic model. In addition, the Young's modulus of nondoped BZY: BaZrO_3 (BZY0), reported by Liu et al. [39], is shown in Figure 4b. The relative density of BZY0 in the researchers' work was fairly high (98.9%), and the influence of porosity was estimated to be only 1%. Therefore, the results of this work and those reported by Hoedl and Liu could be compared, neglecting the influence of porosity. The experimental results obtained in this work and those obtained in Hoedl et al. exhibited a same tendency. The sound velocities gradually decreased as the yttrium concentration increased, and yttrium concentration dependences of velocities for two results were close within a difference of 5%. The sound velocities of the BZY with a yttrium concentration of 10 mol% were the same in both the experiments, with a difference of less than 1%. The similar decrement of Young's and bulk moduli indicate that BZYS themselves become softer to outer forces. The thermal expansion coefficient of yttrium-doped barium zirconates also shows a negative yttrium concentration dependence [33]. The values of BZY10, 15, and 20 in dry Ar atmosphere are 8.78 , 9.25 , and $10.1 \times 10^{-6}\text{ K}^{-1}$, respectively. Therefore, the observed yttrium concentration dependences of elastic properties and thermal expansion coefficient are explained by the chemical bond being weakened due to the introduction of oxygen vacancies. In the literature, the values of hydrated and dehydrated samples were measured [38]. The average value for BZY10 was the same as that obtained in this work, and the extrapolated Young's modulus for BZY20 was only 3.6% smaller than that obtained in this study. These results suggest that BZYS exhibit similar elastic properties, regardless of the materials, synthesis methods, and sintering method and conditions. Although the elastic modulus is a fundamental material property determined by the interatomic potential and is thus expected to be the same, this is the first report that confirms this aspect for low sinterability materials such as BZYS.



(a) Sound velocities



(b) Young's modulus

Figure 4. (a) Ultrasonic longitudinal and sound velocities and (b) Young's modulus at 20 °C as a function of the doped yttrium concentration. The solid and hollow symbols indicate longitudinal and transverse sound velocities, respectively. The circles indicate the experimental values of the as-prepared samples in this study, and the triangles and squares indicate the experimental data of the as-prepared and dehydrated samples reported in existing studies [38,39]. The dashed lines are presented as eye guides.

Subsequently, the samples were heated up to 700 °C, and their characteristics were examined. At 300–400 °C, transverse and longitudinal sound attenuation occurred, and the attenuation was recovered at higher than 400 °C. The attenuation of transverse sound was significant and prevented the accurate determination of the TOF. Therefore, the transverse sound velocities were not used in this range. As the Ag paste became softer as the temperature increased and was partially shrunk due to the sintering of Ag particles in the paste, the interfaces between the sample and the Ag paste were peeled off around 300 °C, and the attenuation occurred around the peeling surface. If an appropriate load could be applied, as in a power generation test, to maintain the gas seal of the molten glass, we would be able to prevent this attenuation, but due to the structure of the apparatus, it is difficult to apply a load greater than the mass of the upper buffer rod. At a temperature higher than 400 °C, the attenuation was recovered, and both sound velocities were again obtained with high accuracy. The interfaces could be recovered due to the applied force from the upper rod because the Ag paste became ever softer.

The longitudinal and transverse sound velocities of BZY0, BZY10, BZY15, and BZY20 measured during the heating are shown in Figure 5. A clear difference in temperature

dependence was observed between doped and nondoped samples. For all doped samples, the velocities exhibited a weak negative dependence on the temperature; specifically, the sound velocities decreased as the temperature increased. In addition, at temperatures higher than 400 °C, the transverse sound velocities for the different samples were considerably different over the influence of the measurement error. By contrast, both sound velocities of BZY0 were almost constant in this temperature range.

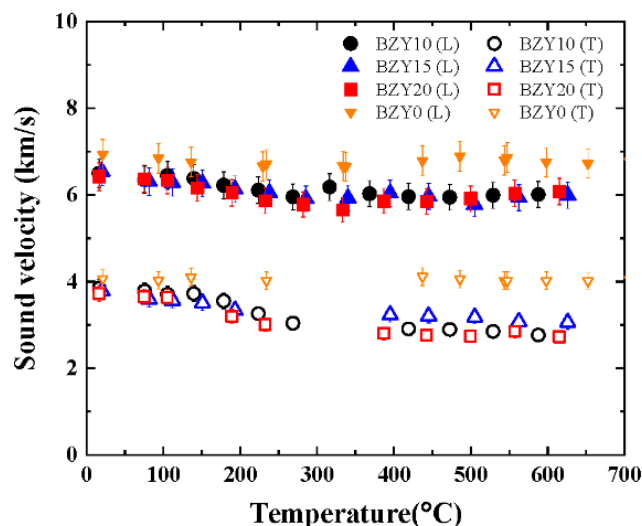


Figure 5. Temperature dependence of ultrasonic longitudinal and transverse sound velocities of BZY0 (orange inverted triangles), BZY10 (black circles), BZY15 (blue triangles), and BZY20 (red squares). The solid and hollow symbols correspond to longitudinal and transverse sound velocities, respectively. Transverse sound velocities in the temperature range of 300–400 °C could not be measured owing to ultrasonic sound attenuation.

The Young's, shear, and bulk moduli and Poisson's ratio calculated using Equations (5)–(8) are shown in Figure 6. As all the properties are calculated based on the square of the transverse sound velocities, the differences between doped and nondoped samples and among the three doped samples at temperatures higher than 400 °C became significant. The elastic properties, as well as the sound velocities, of nondoped BZY0 were almost constant. By contrast, the Young's and shear moduli of doped samples exhibited a nonlinear dependence on the temperature: as the temperature increased, the two moduli exhibited different decrement rates. Specifically, the decrement rates under 100 °C and over 400 °C were similar; however, the decrement rate was high between 100 °C and 300 °C. Consequently, at a temperature higher than 400 °C, the Young's modulus was several tens of percentage points smaller than that at the room temperature. Generally, refractory oxides such as alumina, magnesia, and mullite exhibit a negative linear dependence to the temperature, owing to the nature of the chemical bonds between the atoms at a temperature less than half the corresponding melting temperatures [51]. For example, the decrement rate of Al_2O_3 as the temperature increases from the room temperature to 500 °C is approximately 7%. High-temperature elastic properties for this system were only reported for the Young's modulus of BZY0 measured using the impulse excitation method [39]. BZY0 exhibits a linear decrement in the Young's modulus with an increasing temperature in the range of room temperature to 700 °C, with the decrement rate being 7%. Therefore, the observed constant of the Young's and share moduli of BZY0 is considered to result from the nature of chemical bonds in nondoped barium zirconate.

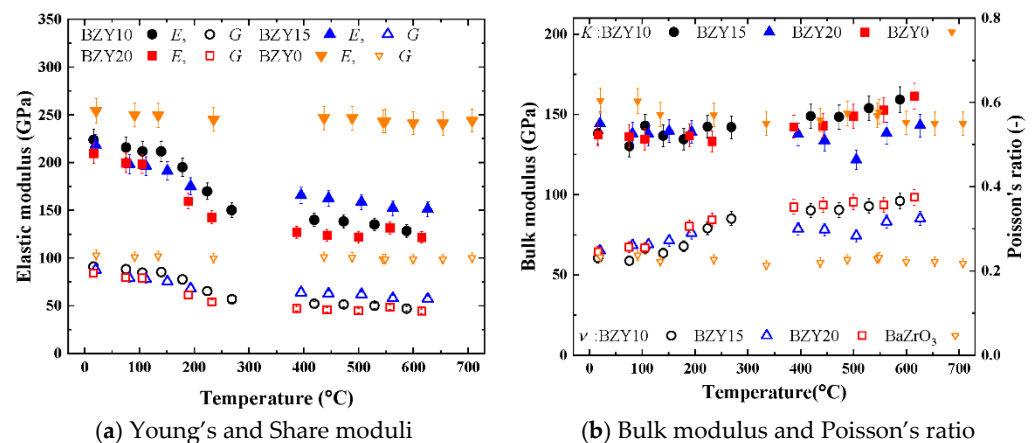


Figure 6. Elastic modulus of BZY0 (orange inverted triangles), BZY10 (black circles), BZY15 (blue triangles), and BZY20 (red squares) as a function of the temperature. (a) The Young's (E) and shear (G) moduli are indicated as solid and hollow symbols, respectively. (b) The bulk modulus (K) and Poisson ratios (ν) are indicated by solid and hollow symbols, respectively. Some data points in the temperature range of 300–400 °C were removed, as the transverse sound velocities could not be measured in this range with high accuracy due to the weakling of the adhesive Ag paste.

The decrement for doped BZY10, BZY15, and BZY20 was considerably larger than that of BZY0. Doped ceramics, which are widely used in the field of solid-state ionics, also exhibit the same nonlinear temperature dependences as doped BZYS. For example, mixed electronic and ionic conductors such as $\text{La}_{0.6}\text{Sr}_{0.4}\text{Co}_{1-y}\text{Fe}_y\text{O}_{3-\delta}$ exhibit a large increment of Young's modulus over several tens of %, owing to a phase transformation. In fact, even in the case of 8YSZ, which is not expected to undergo a phase transformation in the short term, the Young's modulus first decreases with an increase in the temperature and later increases [52,53]. The Young's modulus of 8YSZ decreases as the temperature increases and exhibits a local minimum at approximately 500 °C. The difference between the values at the room temperature and the local minimum is more than 30%. The behavior of 8YSZ is explained by the change in the local crystal symmetry: as 8YSZ has both cubic metastable and tetragonal stable phases, the metastable phase gradually changes to stable phases in the intermediate temperature range [53]. Nevertheless, Gd-doped ceria, which has a fully cubic phase, does not exhibit a nonlinear temperature dependence similar to that observed for 8YSZ. Hence, it is assumed that the Young's modulus does not change considerably if no local change occurs in the crystal symmetry. As BZY0 has a stable cubic phase in the temperature range of 20–700 °C, the observed constant elastic moduli of BZY0 supports this estimation.

As doped BZYS involve a stable cubic phase, they were expected to behave similarly to nondoped BZY0. In contrast, the behavior of the doped BZYS was similar to that of 8YSZ. This phenomenon likely relates to defect structures that consist of oxygen vacancy and substituted yttrium and hydration, in which protons are introduced to lattices caused by the existence of the defect structures. The host lattice of BZYS is BaZrO_3 , whose tolerance factor is approximately 1 [54]. However, the lattices in which the tetravalent zirconium is replaced by a larger trivalent yttrium exhibit a tolerance factor of 0.92, which is close to the lower limit of the range of cubic crystal symmetry. The relatively negatively charged yttrium at the Zr site in the lattice is also considered to be preferentially coordinated by oxygen vacancies with relatively positive charges [55]. Around the oxygen vacancy in the lattice, lattice volume tends to expand due to the lack of Coulomb force. Hence, it is reasonable to assume that the lattice involving yttrium tends to have a locally decreased symmetry, and local symmetry changes as temperature changes. On the other hand, hydration occurs in perovskite-type proton conductors, such as doped barium zirconate and strontium zirconate. In the process, barium zirconate reacts with water molecules in the atmosphere, and two hydrogens and one oxygen are introduced into the lattice.

Oxygen occupies the oxygen vacancy, and protons are located in interstitial sites near the oxygen. The hydration causes lattice expansion. As the hydration is an exothermic process, the progress of hydration depends on the temperature and water vapor pressure in the atmosphere [33,41,56]. According to previously obtained results, in the case of well-sintered BZY15, at approximately 800 °C, proton concentration is considered to be zero under thermal equilibrium conditions. The hydration progresses as the temperature decreases, and the proton concentration increases. The proton concentration at 500 °C is 7 mol%, and the value reaches 80% of the yttrium concentration under high humidity atmospheres (12 mol%). According to the case of BZY15 in Anderson et al., full hydration (all oxygen vacancy is occupied by oxygen) causes 0.4% lattice expansion, and the expansion suggests that the lattices in which oxygen vacancy is occupied by hydration are locally expanded strongly. Both of them are considered to be reasonable explanations for the cause of a local symmetry change. Therefore, two hypotheses were formed: the first hypothesis was that the temperature dependence of the elastic properties was a result of the inherent nature of doped barium zirconate as in the case of 8YSZ and Sc and Ce co-doped ZrO₂ [53]. Locally decreased symmetry might recover again as the temperature increases. The second hypothesis was that the temperature dependence of the elastic properties was a result of the oxygen vacancy occupation caused by hydration. Ultrasonic measurement was performed under the laboratory air, which includes low humidity, and the samples were kept at each temperature at least 20 min. Therefore, hydration and dehydration could occur during the measurement and cause a local symmetry change. However, because this study used dense and thick pellet shaped samples, it was certain that the rate of hydration and de-hydration was slower than that in small bars and powders often used for thermos-gravimetric and electrical conductivity measurements. In fact, the lattice constants of the sample before and after the measurement did not actually change significantly. If the hydration progressed during the measurement, protons were introduced into the lattice, and lattice constants became larger than those before the measurement. Thus, the rate of hydration during the measurement was considered to be low. At present, the observed temperature dependences may be due to the nature of doped BZYs and independent to hydration. However, if we can control the hydration rate and measure elastic properties, the observed temperature dependence might be expected to differ from the results in this paper and change as hydration progresses.

4. Conclusions

We examined the temperature dependence of the elastic properties of BZYs with various yttrium concentrations, which are promising proton-conducting solid electrolytes for PCFCs. A novel evaluation method for low sinterability materials such as BZYs was established based on the conventional ultrasonic method using two buffer rods, and the elastic properties of BZYs at the SOFC operating temperature of 700 °C were determined by using small-pellet-type samples. The Young's and shear moduli exhibited a rapid decrement (30–40%) as the temperature increased from the room temperature to the operating temperature.

Future work must examine whether the decrement in the elastic properties is a phenomenon peculiar to doped oxides for SOFC materials such as 8YSZ or if it is due to the influence of hydration, which is specific to proton conductors. As this decrement influences mechanical stability and reliability, an in-depth examination of the high-temperature elastic properties of PCFC materials is required.

Supplementary Materials: The following are available online at <https://www.mdpi.com/article/10.3390/met11060968/s1>, Figure S1: Dependence of the sound velocity on the porosity of 8YSZ, determined experimentally.

Author Contributions: Conceptualization, F.I.; methodology, K.H.; validation, F.I. and K.H.; formal analysis, K.H.; investigation, K.H.; resources, F.I.; data curation, K.H.; writing—original draft preparation, F.I. and K.H.; writing—review and editing, F.I.; supervision, F.I.; project administration, F.I.; funding acquisition, F.I. All authors have read and agreed to the published version of the manuscript.

Funding: This research was partially funded by EIG-CONCERT-Japan, Strategic International Collaborative Research Program, Japan Science and Technology Agency.

Institutional Review Board Statement: Not applicable.

Informed Consent Statement: Not applicable.

Acknowledgments: The authors would like to acknowledge helpful discussion with the member of “DAICHI” in EIG-CONCERT-Japan.

Conflicts of Interest: The authors declare no conflict of interest. The funders had no role in the design of the study; in the collection, analyses, or interpretation of data; in the writing of the manuscript; or in the decision to publish the results.

References

1. Kreuer, K.D. On the development of proton conducting materials for technological applications. *Solid State Ion.* **1997**, *97*, 1–15. [[CrossRef](#)]
2. Duan, C.C.; Tong, J.H.; Shang, M.; Nikodemski, S.; Sanders, M.; Ricote, S.; Almansoori, A.; O’Hayre, R. Readily processed protonic ceramic fuel cells with high performance at low temperatures. *Science* **2015**, *349*, 1321–1326. [[CrossRef](#)] [[PubMed](#)]
3. Kreuer, K.D. On the complexity of proton conduction phenomena. *Solid State Ion.* **2000**, *136–137*, 149–160. [[CrossRef](#)]
4. Iguchi, F.; Sata, N.; Yugami, H. Proton transport properties at the grain boundary of barium zirconate based proton conductors for intermediate temperature operating SOFC. *J. Mater. Chem.* **2010**, *20*, 6265–6270. [[CrossRef](#)]
5. Bae, K.; Jang, D.Y.; Choi, H.J.; Kim, D.; Hong, J.; Kim, B.-K.; Lee, J.-H.; Son, J.-W.; Shim, J.H. Demonstrating the potential of yttrium-doped barium zirconate electrolyte for high-performance fuel cells. *Nat. Commun.* **2017**, *8*, 14553. [[CrossRef](#)] [[PubMed](#)]
6. Kochetova, N.; Animitsa, I.; Medvedev, D.; Demin, A.; Tsiakaras, P. Recent activity in the development of proton-conducting oxides for high-temperature applications. *RSC Adv.* **2016**, *6*, 73222–73268. [[CrossRef](#)]
7. Iguchi, F.; Yamane, T.; Kato, H.; Yugami, H. Low temperature fabrication of an anode-supported SOFC with a proton-conducting electrolyte based on lanthanum scandate using a PLD method. *Solid State Ion.* **2015**, *275*, 117–121. [[CrossRef](#)]
8. Stange, M.; Stefan, E.; Denonville, C.; Larring, Y.; Rørvik, P.M.; Haugsrud, R. Development of novel metal-supported proton ceramic electrolyser cell with thin film BZY15–Ni electrode and BZY15 electrolyte. *Int. J. Hydrog. Energy* **2017**, *42*, 13454–13462. [[CrossRef](#)]
9. Sata, N.; Shibata, Y.; Iguchi, F.; Yugami, H. Crystallization process of perovskite type oxide thin films deposited by PLD without substrate heating: Influence of sputtering rate and densification-driven high tensile strain. *Solid State Ion.* **2015**, *275*, 14–18. [[CrossRef](#)]
10. Liu, J.; Iguchi, F.; Sata, N.; Yugami, H. Optical absorption of Sr-doped LaScO₃ single crystals. *Solid State Ion.* **2007**, *178*, 521–526. [[CrossRef](#)]
11. Oishi, M.; Akoshima, S.; Yashiro, K.; Sato, K.; Mizusaki, J.; Kawada, T. Defect structure analysis of B-site doped perovskite-type proton conducting oxide BaCeO₃ Part 2: The electrical conductivity and diffusion coefficient of BaCe_{0.9}Y_{0.1}O_{3-delta}. *Solid State Ion.* **2008**, *179*, 2240–2247. [[CrossRef](#)]
12. Oishi, M.; Akoshima, S.; Yashiro, K.; Sato, K.; Mizusaki, J.; Kawada, T. Defect structure analysis of B-site doped perovskite-type proton conducting oxide BaCeO₃ Part 1: The defect concentration of BaCe_{0.9}M_{0.1}O_{3-delta} (M = Y and Yb). *Solid State Ion.* **2009**, *180*, 127–131. [[CrossRef](#)]
13. Okuyama, Y.; Okuyama, K.; Mizutani, Y.; Sakai, T.; Lee, Y.S.; Matsumoto, H. Proton transport properties of La_{0.9}Sr_{0.1}Yb_{0.8}In_{0.2}O_{3-delta} and its application to proton ceramic fuel cell. *Int. J. Hydrog. Energy* **2014**, *39*, 20829–20836. [[CrossRef](#)]
14. Okuyama, Y.; Ymaguchi, T.; Matsunaga, N.; Sakai, G. Proton Conduction and Incorporation into La_{1-x}Ba_xYb_{0.5}In_{0.5}O_{3-delta}. *Mater. Trans.* **2018**, *59*, 14–18. [[CrossRef](#)]
15. Kato, H.; Iguchi, F.; Yugami, H. Compatibility and performance of La_{0.675}Sr_{0.325}Sc_{0.99}Al_{0.01}O₃ perovskite-type oxide as an electrolyte material for SOFCs. *Electrochemistry* **2014**, *82*, 845–850. [[CrossRef](#)]
16. Ishiyama, T.; Kishimoto, H.; Develos-Bagarinao, K.; Yamaji, K.; Yamaguchi, T.; Fujishiro, Y. Dissociation behavior of protons incorporated in yttrium doped barium zirconate. *J. Solid State Chem.* **2017**, *252*, 22–27. [[CrossRef](#)]
17. Ishiyama, T.; Kishimoto, H.; Develos-Bagarinao, K.; Yamaji, K.; Yamaguchi, T.; Fujishiro, Y. Correlation between Dissolved Protons in Nickel-Doped BaZr_{0.1}Ce_{0.7}Y_{0.1}Yb_{0.1}O_{3-delta} and Its Electrical Conductive Properties. *Inorg. Chem.* **2017**, *56*, 11876–11882. [[CrossRef](#)]
18. Kawada, T.; Watanabe, S.; Hashimoto, S.; Sakamoto, T.; Unemoto, A.; Kurumatani, M.; Sato, K.; Iguchi, F.; Yashiro, K.; Amezawa, K.; et al. Classification of mechanical failures of SOFC and strategy for evaluation of the operational margins. *ECS Trans.* **2009**, *25*, 467–472. [[CrossRef](#)]

19. Muramatsu, M.; Terada, K.; Kawada, T.; Yashiro, K.; Takahashi, K.; Takase, S. Characterization of time-varying macroscopic electro-chemo-mechanical behavior of SOFC subjected to Ni-sintering in cermet microstructures. *Comput. Mech.* **2015**, *56*, 653–676. [[CrossRef](#)]
20. Chou, Y.-S.; Stevenson, J.W.; Armstrong, T.R.; Pederson, L.R. Mechanical Properties of $\text{La}_{1-x}\text{Sr}_x\text{Co}_{0.2}\text{Fe}_{0.8}\text{O}_3$ Mixed-Conducting Perovskites Made by the Combustion Synthesis Technique. *J. Am. Ceram. Soc.* **2000**, *83*, 1457–1464. [[CrossRef](#)]
21. Atkinson, A.; Selcuk, A. Mechanical behavior of ceramic oxygen ion-conducting membranes. *Solid State Ion.* **2000**, *134*, 59–66. [[CrossRef](#)]
22. Atkinson, A. Chemically-induced stresses in gadolinium-doped ceria solid oxide fuel cell electrolytes. *Solid State Ion.* **1997**, *95*, 249–258. [[CrossRef](#)]
23. Giraud, S.; Canel, J. Young's modulus of some SOFCs materials as a function of temperature. *J. Eur. Ceram. Soc.* **2008**, *28*, 77–83. [[CrossRef](#)]
24. Laurencin, J.; Delette, G.; Lefebvre-Joud, F.; Dupeux, A. A numerical tool to estimate SOFC mechanical degradation: Case of the planar cell configuration. *J. Eur. Ceram. Soc.* **2008**, *28*, 1857–1869. [[CrossRef](#)]
25. Laurencin, J.; Delette, G.; Usseglio-Viretta, F.; Di Iorio, S. Creep behaviour of porous SOFC electrodes: Measurement and application to Ni-8YSZ cermets. *J. Eur. Ceram. Soc.* **2011**, *31*, 1741–1752. [[CrossRef](#)]
26. Iguchi, F.; Akrasevee, S.; Miyoshi, Y. Influence of NiO reduction on residual strain in NiO/Ni-YSZ. *Mater. Trans.* **2018**, *59*, 27–32. [[CrossRef](#)]
27. Watanabe, S.; Sato, K.; Takeyama, Y.; Iguchi, F.; Yashiro, K.; Amezawa, K.; Yugami, H.; Hashida, T.; Mizusaki, J.; Kawada, T. Mechanical properties evaluation method for non-stoichiometric materials under high temperature and oxidizing/reducing conditions. *Trans. Jpn Soc. Mech. Eng. A* **2011**, *77*, 1357–1366. [[CrossRef](#)]
28. Ishida, T.; Iguchi, F.; Sato, K.; Hashida, T.; Yugami, H. Fracture properties of $(\text{CeO}_2)_{1-x}(\text{RO}_{1.5})_x$ (R = Y, Gd, and Sm; X = 0.02–0.20) ceramics. *Solid State Ion.* **2005**, *176*, 2417–2421. [[CrossRef](#)]
29. Sameshima, S.; Ichikawa, T.; Kawaminami, M.; Hirata, Y. Thermal and mechanical properties of rare earth-doped ceria ceramics. *Mater. Chem. Phys.* **1999**, *61*, 31–35. [[CrossRef](#)]
30. Lyagaeva, Y.G.; Medvedev, D.A.; Demin, A.K.; Tsiakaras, P.; Reznitskikh, O.G. Thermal expansion of materials in the barium cerate-zirconate system. *Phys. Solid State* **2015**, *57*, 285–289. [[CrossRef](#)]
31. Hayashi, H.; Saitou, T.; Maruyama, N.; Inaba, H.; Kawamura, K.; Mori, M. Thermal expansion coefficient of yttria stabilized zirconia for various yttria contents. *Solid State Ion.* **2005**, *176*, 613–619. [[CrossRef](#)]
32. Andersson, A.K.E.; Selbach, S.M.; Knee, C.S.; Grande, T. Chemical Expansion Due to Hydration of Proton-Conducting Perovskite Oxide Ceramics. *J. Am. Ceram. Soc.* **2014**, *97*, 2654–2661. [[CrossRef](#)]
33. Han, D.L.; Hatada, N.; Uda, T. Chemical Expansion of Yttrium-Doped Barium Zirconate and Correlation with Proton Concentration and Conductivity. *J. Am. Ceram. Soc.* **2016**, *99*, 3745–3753. [[CrossRef](#)]
34. Han, F.; Zhou, X.; Dayaghi, A.M.; Norby, T.; Stange, M.; Sata, N.; Costa, R. Development of Metal Supported Cells Using BaZrO_3 -Based Proton Conducting Ceramics. *ECS Trans.* **2019**, *91*, 1035–1045. [[CrossRef](#)]
35. Stange, M.; Dayaghi, A.M.; Denonville, C.; Larring, Y.; Rørvik, P.M.; Haugsrud, R.; Norby, T. Fabrication of Metal-Supported Proton-Conducting Electrolysers with Thin Film Sr- and Ce-Doped BZY Electrolyte. *ECS Trans.* **2019**, *91*, 941–949. [[CrossRef](#)]
36. Sakai, T.; Kato, T.; Katsui, H.; Tanaka, Y.; Goto, T. Preparation of Y-doped BaZrO_3 thin film electrolyte by laser chemical vapor deposition. *Mater. Today Commun.* **2020**, *24*, 101184. [[CrossRef](#)]
37. Dubois, A.; Taghikhani, K.; Berger, J.R.; Zhu, H.; O'Hayre, R.P.; Braun, R.J.; Kee, R.J.; Ricote, S. Chemo-Thermo-Mechanical Coupling in Protonic Ceramic Fuel Cells from Fabrication to Operation. *J. Electrochem. Soc.* **2019**, *166*, F1007–F1015. [[CrossRef](#)]
38. Hoedl, M.F.; Makagon, E.; Lubomirsky, I.; Merkle, R.; Kotomin, E.A.; Maier, J. Impact of point defects on the elastic properties of BaZrO_3 : Comprehensive insight from experiments and ab initio calculations. *Acta Mater.* **2018**, *160*, 247–256. [[CrossRef](#)]
39. Liu, Y.; Zhang, W.; Wang, B.; Sun, L.; Li, F.; Xue, Z.; Zhou, G.; Liu, B.; Nian, H. Theoretical and experimental investigations on high temperature mechanical and thermal properties of BaZrO_3 . *Ceram. Int.* **2018**, *44*, 16475–16482. [[CrossRef](#)]
40. Iguchi, F.; Sata, N.; Tsurui, T.; Yugami, H. Microstructures and grain boundary conductivity of $\text{BaZr}_{1-x}\text{Y}_x\text{O}_3$ (x = 0.05, 0.10, 0.15) ceramics. *Solid State Ion.* **2007**, *178*, 691–695. [[CrossRef](#)]
41. Kreuer, K.D. Proton-conducting oxides. *Annu. Rev. Mater. Res.* **2003**, *33*, 333–359. [[CrossRef](#)]
42. Bi, L.; Traversa, E. Synthesis strategies for improving the performance of doped- BaZrO_3 materials in solid oxide fuel cell applications. *J. Mater. Res.* **2014**, *29*, 1–15. [[CrossRef](#)]
43. Zhong, Z.M. Stability and conductivity study of the $\text{BaCe}_{0.9-x}\text{Zr}_x\text{Y}_{0.1}\text{O}_{2.95}$ systems. *Solid State Ion.* **2007**, *178*, 213–220. [[CrossRef](#)]
44. Iguchi, F.; Endo, Y.; Ishida, T.; Yokobori, T.; Yugami, H.; Otake, T.; Kawada, T.; Mizusaki, J. Oxygen partial pressure dependence of creep on yttria-doped ceria ceramics. *Solid State Ion.* **2005**, *176*, 641–644. [[CrossRef](#)]
45. Sather, A. Ultrasonic Buffer-Rod Technique for High-Temperature Measurement of Elastic Moduli of Short Specimens. *J. Acoust. Soc. Am.* **1968**, *43*, 1291–1294. [[CrossRef](#)]
46. Babilo, P.; Haile, S.M. Enhanced sintering of yttrium-doped barium zirconate by addition of ZnO. *J. Am. Ceram. Soc.* **2005**, *88*, 2362–2368. [[CrossRef](#)]
47. Hinata, K.; Iguchi, F. Elastic Properties of Yttrium Doped Barium Zirconate. *ECS Trans.* **2019**, *91*, 1065–1073. [[CrossRef](#)]
48. Iguchi, F.; Tsurui, T.; Sata, N.; Nagao, Y.; Yugami, H. The relationship between chemical composition distributions and specific grain boundary conductivity in Y-doped BaZrO_3 proton conductors. *Solid State Ion.* **2009**, *180*, 563–568. [[CrossRef](#)]

49. Redwood, M. *Mechanical Waveguides*; Pergamon Press: Oxford, UK, 1960.
50. Fukuhara, M.; Sanpei, A. High Temperature-Elastic Moduli and Internal Dilational and Shear Frictions of Fused Quartz. *JPN J. Appl. Phys.* **1994**, *33*, 2890–2893. [[CrossRef](#)]
51. Anderson, O.L.; Isaak, D.; Oda, H. High-Temperature Elastic-Constant Data on Minerals Relevant to Geophysics. *Rev. Geophys.* **1992**, *30*, 57–90. [[CrossRef](#)]
52. Kimura, Y.; Kushi, T.; Hashimoto, S.; Amezawa, K.; Kawada, T. Influences of Temperature and Oxygen Partial Pressure on Mechanical Properties of La_{0.6}Sr_{0.4}Co_{1-y}FeyO_{3-d}. *J. Am. Ceram. Soc.* **2012**, *95*, 2608–2613. [[CrossRef](#)]
53. Kushi, T.; Sato, K.; Unemoto, A.; Hashimoto, S.; Amezawa, K.; Kawada, T. Elastic modulus and internal friction of SOFC electrolytes at high temperatures under controlled atmospheres. *J. Power Sources* **2011**, *196*, 7989–7993. [[CrossRef](#)]
54. Goldschmidt, V.M. Die Gesetze der Krystallochemie. *Naturwissenschaften* **1926**, *14*, 477–485. [[CrossRef](#)]
55. Björketun, M.E.; Sundell, P.G.; Wahnström, G. Structure and thermodynamic stability of hydrogen interstitials in BaZrO₃ perovskite oxide from density functional calculations. *Faraday Discuss* **2007**, *134*, 247–265. [[CrossRef](#)] [[PubMed](#)]
56. Iguchi, F.; Nagao, Y.; Sata, N.; Yugami, H. Proton concentration in 15 mol% Y-doped BaZrO₃ proton conductors prepared at various temperatures. *Solid State Ion.* **2011**, *192*, 97–100. [[CrossRef](#)]